ADVANCED MATERIALS
www.advmat.de

Engineering Electro-Optic $BaTiO_3$ Nanocrystals via Efficient Doping

*Sasa Wang, Tong Zhu, Randy Sabatini, Amin Morteza Najarian, Muhammad Imran, Ruyan Zhao, Pan Xia, Lewei Zeng, Sjoerd Hoogland, Dwight S. Seferos, and Edward H. Sargent**

Electro-optic (EO) modulators provide electrical-to-optical signal conversion relevant to optical communications. Barium titanate ($BaTiO_3$) is a promising material system for EO modulation in light of its optical ultrafast nonlinearity, low optical loss, and high refractive index. To enhance further its spontaneous polarization, $BaTiO_3$ can be doped at the Ba and Ti sites; however, doping is often accompanied by ion migration, which diminishes EO performance. Here, donor–acceptor doping and its effect on EO efficiency are investigated, finding that La-doped $BaTiO_3$ achieves an EO coefficient of 42 pm V^{-1} at 1 kHz, fully twice that of the pristine specimen; however, it is also observed that, with this single-element doping, the EO response falls off rapidly with frequency. From impedance spectroscopy, it is found that frequency-dependent EO is correlated with ion migration. Density functional theory calculations predict that the ion-migration barrier decreases with La^{3+} doping but can be recovered with further Mn^{2+} doping, a finding that prompts to prevent ion migration by incorporating Mn^{2+} into the Ti-site to compensate for the charge imbalance.

1. Introduction

Electro-optic (EO) modulators convert electric signals into optical pulses relevant to communications.[1] Owing to a lack of inversion symmetry, nonlinear optical crystals exhibit an optical anisotropy that is proportional to the electric field, resulting in a linear EO effect.[2] This effect, also known as the Pockels effect, is frequency-dependent, and it is desirable that modulators operate at high frequencies. With the rapid increase in the complexity and capacity of data in networks, research on EO materials has been focused on improving bandwidth and minimizing power consumption. Photonic nanostructures and thin films are prime candidates to meet these requirements.

Barium titanate ($BaTiO_3$) is a ferroelectric with a large Pockels coefficient, low optical loss, and fast response.[3] However, it remains challenging to integrate the $BaTiO_3$ materials with photonic structures on a single chip because of the mismatch of the crystal properties with the photonic structure, which renders attempts at heterogenous integration costly and complex.

$BaTiO_3$ nanoparticles, processed from solution, allow uniform films to be integrated onto photonic structures via wet deposition methods, such as spin coating, drop casting, and spray pyrolysis, thereby simplifying the manufacturing process of on-chip EO modulators.[4] When the particle size is reduced in this way, however, a lower EO response is seen.[5]

We investigated whether doping could overcome the limitations of solution-processed ABO_3- perovskite nanoparticles such as $BaTiO_3$.[6] Rare-earth ions such as La^{3+} and Er^{3+} have been used to substitute the Ba site as donors, while transition metals Mn^{2+} and Ni^{2+} favor the Ti site as acceptors. Both donor and acceptor doping have been studied in view of their potential to improve the dielectric constant and spontaneous polarization.[7] Since EO response is proportional to spontaneous polarization and dielectric constant,[8] doping appears to have the potential to enhance EO.

2. Results and Discussion

We used an ethanol dispersion with 20 wt% of $BaTiO_3$ nanoparticles to fabricate films (Experimental Section). The average nanoparticle diameter is 200 nm, sufficient to support the tetragonal phase.[9] We used atomic force microscopy (AFM) to measure the surface topography and thickness of the $BaTiO_3$ nanoparticle films: this revealed a thickness of 700 nm and a root-mean-square of 25 nm (Figure S1, Supporting Information). The optical transmission spectra of the $BaTiO_3$ nanoparticle films were recorded using a UV–vis–NIR (near-infrared) spectrometer (Figure S2a, Supporting Information). Spin-cast films exhibit transmission of 85% in the wavelength range between 400 and 2000 nm. The refractive index of the

S. Wang, T. Zhu, R. Sabatini, A. M. Najarian, M. Imran, P. Xia, L. Zeng, S. Hoogland, E. H. Sargent
Department of Electrical and Computer Engineering
University of Toronto
10 King's College Road, Toronto, Ontario M5S 3G4, Canada
E-mail: ted.sargent@utoronto.ca
R. Zhao, D. S. Seferos
Department of Chemistry
University of Toronto
80 St. George Street, Toronto, Ontario M5S 3H6, Canada
The ORCID identification number(s) for the author(s) of this article can be found under https://doi.org/10.1002/adma.202207261.

DOI: 10.1002/adma.202207261

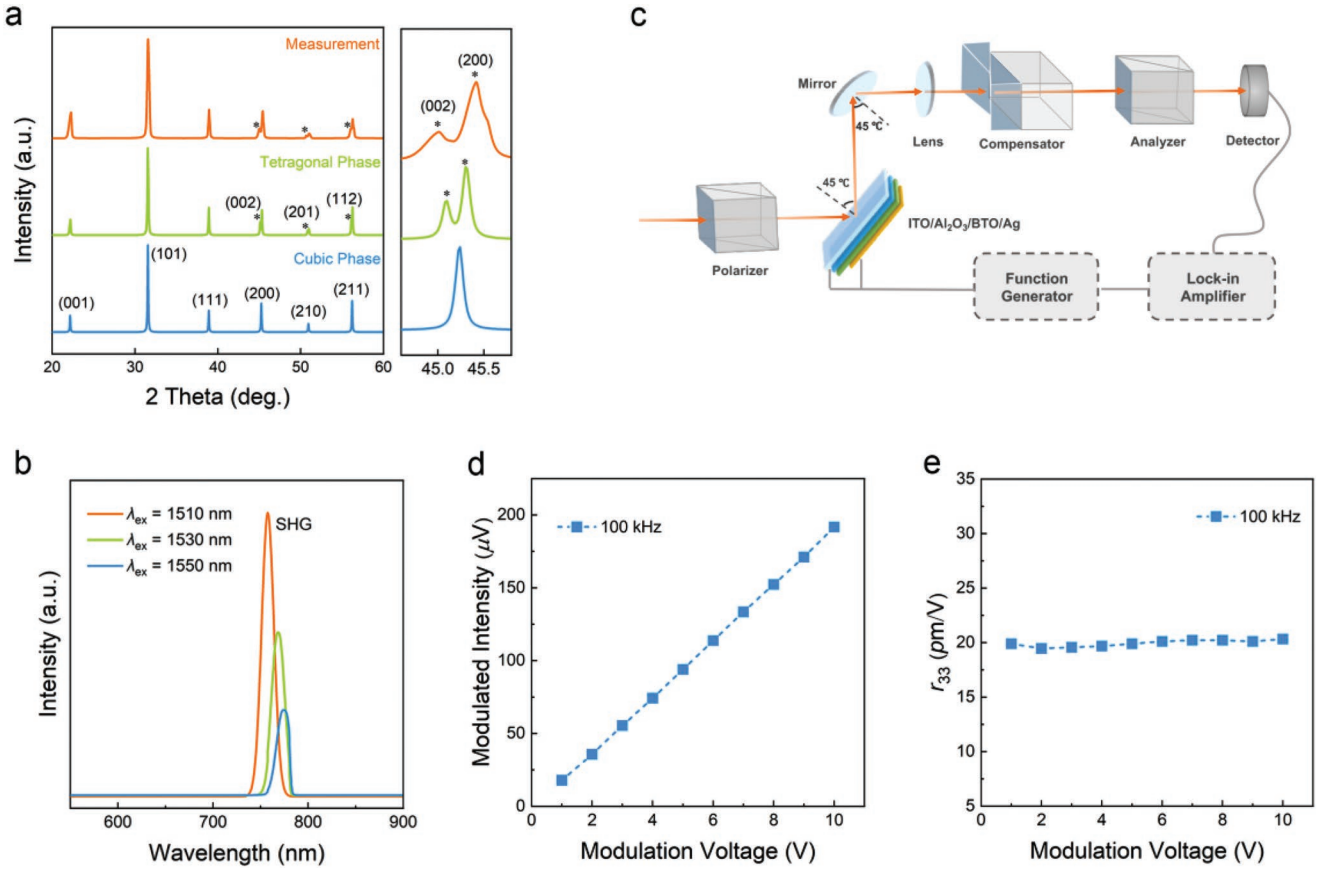

Figure 1. a) Comparison of the powder XRD patterns of 200 nm $BaTiO_3$ nanoparticle films and the tetragonal and cubic phases. b) SHG of the 200 nm $BaTiO_3$ nanoparticle films at excitation wavelengths of 1510, 1530, and 1550 nm. c) Schematic of the ellipsometry setup used in the EO measurement. d) Observed linear increase in reflected light intensity and the modulation voltage of the $BaTiO_3$ nanoparticle films, indicative of a linear EO effect. e) EO coefficient as a function of the AC voltage at a frequency of 100 kHz.

nanoparticle films is measured to be 1.65 at 1.55 μm (Figure S3, Supporting Information), which is comparable to that observed previously in $BaTiO_3$ nanoparticles.[4b]

We used X-ray diffraction (XRD) to characterize the structure of the $BaTiO_3$ nanoparticle films and compared the XRD patterns with the tetragonal (noncentrosymmetric) and cubic (centrosymmetric) phases (**Figure 1**a). The splitting of the (001)/(100), (002)/(200), (102)/(210), and the (112)/(211) diffraction peaks is consistent with the tetragonal phase, indicating a noncentrosymmetric structure. This is further supported by selected area electron diffraction and high-resolution transmission electron microscopy (HRTEM) (Figures S4 and S5, Supporting Information).

We next performed second-harmonic generation (SHG) measurements to verify its noncentrosymmetric structure (Figure 1b). Under a femtosecond laser irradiation, clear SHG signals are observed for $BaTiO_3$ nanoparticle films. As we shifted the excitation wavelength from 1550 to 1510 nm, the peak intensity increased and the peak position blueshifted, revealing the second-order optical nonlinearity. The SHG signals confirm the noncentrosymmetric structure of the unpoled $BaTiO_3$ nanoparticle films, linked to multiaxial ferroelectric properties.[10]

We characterized the linear EO effect of the $BaTiO_3$ nanoparticle films using the Teng–Man method in reflection mode at 1.55 μm.[11] We used a device configuration of indium tin oxide (ITO)/Al_2O_3/$BaTiO_3$/Ag, and the schematic of the ellipsometry setup used for the EO measurement is shown in Figure 1c. A 1.55 μm laser beam is incident on the back of the ITO-coated glass substrate at an angle θ, and back-reflected by the top silver electrode. The polarization of the input beam is set at 45° to the incident plane so that the parallel (*s*-wave) and perpendicular (*p*-wave) components of the optical field are of equal amplitude. The reflected beam propagates from the sample through a Soleil–Babinet compensator to tune the phase retardation between the *s*- and *p*-component, passes through an analyzer, and finally is detected by a Ge NIR photodetector connected to a lock-in amplifier. The applied electrical field (V_{pp}) is modulated at frequencies that are tunable up to 10 MHz. The detected intensity of the reflected beam increases linearly with the applied AC voltage (Figure 1d), corresponding to the linear EO effect.

The linear EO effect is estimated from the change of the refractive index with an applied alternating electric field, E

$$\Delta n = \frac{1}{2} r_e n^3 E \tag{1}$$

where r_e is the EO coefficient under a certain electric field. r_e (r_{33}) was then calculated with the following equation[12]

$$r_{33} = \frac{3\lambda I_{ac}}{4\pi V_{ac} I_c n^2} \frac{\left(n^2 - \sin^2\theta\right)^{3/2}}{\left(n^2 - 2\sin^2\theta\right)} \frac{1}{\sin^2\theta} \quad (2)$$

where $\theta = 45°$, $V_{ac} = V_{pp} \sin\theta$, and I_{ac} and I_c represent the amplitude of the modulated light intensity and half-intensity of the dc output, respectively. Using this method, we measured the EO coefficient of undoped $BaTiO_3$ nanoparticles to be 20 pm V^{-1} at 100 kHz (Figure 1e). The EO coefficient is independent of the operating voltage, indicating that the measured signal corresponds to a pure second-order EO process.

We also built ITO/poly(methyl methacrylate) (PMMA)/Ag and ITO/Al_2O_3/Ag thin film devices to examine the effect of reflection from the ITO electrode on the EO coefficient. The PMMA and Al_2O_3-only devices show negligible signals with values comparable to background levels (Figure S6, Supporting Information), indicating that the reflectance of the ITO electrode does not materially contribute to the EO coefficient.

Rare earth doping in ABO_3 perovskite nanoparticles such as $BaTiO_3$ offers an opportunity in enhancing the EO response. We calculated the Berry phase polarization of rare-earth (dopants: La, Ce, Nd, Eu)-doped $BaTiO_3$. La doping is predicted to offer the highest polarization of 30.84 Debye (Figure S7a, Supporting Information). This prompted us to explore La^{3+} as a donor dopant in our studies, aimed at increasing EO performance in $BaTiO_3$ nanoparticle films.

The La-doped $Ba_{1-x}La_xTiO_3$ (x = 0.03, 0.05, 0.065, 0.08, 0.1) nanoparticle films were made by dissolving stoichiometric lanthanum (III) chloride heptahydrate and $BaTiO_3$ nanoparticles in ethanol. The mixed solutions were ultrasonicated for 60 min to disperse evenly and then spin-coated onto the substrate with a speed of 2000 rpm for 30 s, followed by annealing at 250 °C for 30 min.

The well-defined XRD patterns denote a single-phase perovskite structure without any impurity, indicating La has been diffused into the $BaTiO_3$ lattice (Figure S8a, Supporting Information). With increasing La concentration, the (001) diffraction peak shifted toward higher 2θ values (**Figure 2**a), something we attribute to the smaller ionic radius of La^{3+} (≈1.15 Å) compared to Ba^{2+} (1.35 Å).[13]

We used X-ray photoelectron spectroscopy (XPS) to study the surface components of La-doped $BaTiO_3$ nanoparticle films (Figure 2b and Figure S9, Supporting Information). High-resolution spectra of Ba 3d and Ti 2p exhibit no peak shift, and the binding energy remains unchanged after doping. However, the binding energy of O 1s deviates to a higher value, indicating a difference in oxygen vacancy concentration between the undoped and La-doped $BaTiO_3$ nanoparticle films.[14]

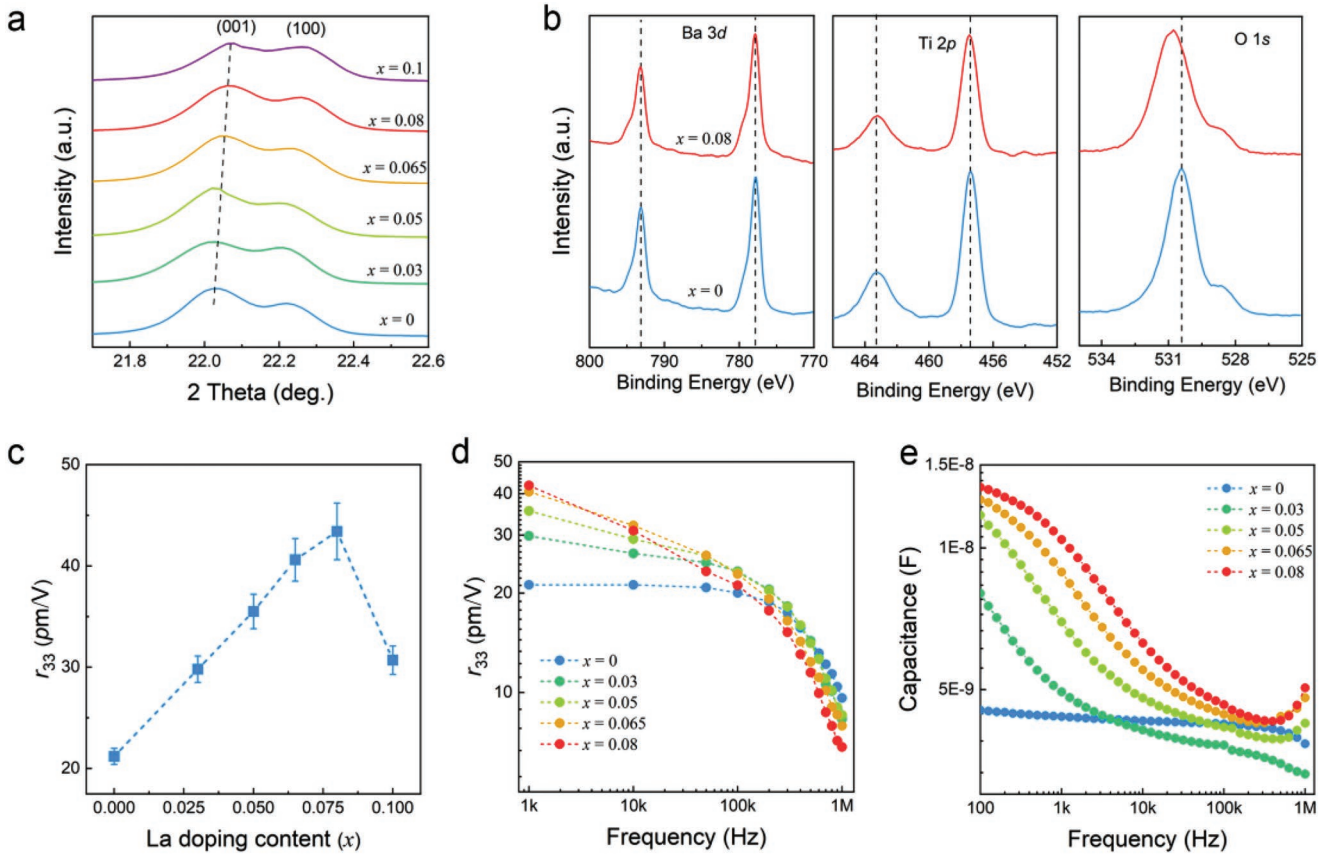

Figure 2. Structural characterization and linear EO performance of La-doped $BaTiO_3$ nanoparticle films. a) Comparison of the XRD patterns of La-doped and undoped $BaTiO_3$ nanoparticle films. The shift to higher 2θ angles indicates the incorporation of La into the crystal lattice. b) Comparison of high-resolution XPS spectra of Ba 3d, Ti 2p, and O 1s for the pristine and x = 0.08 specimen. c) Evolution of the EO coefficient with La concentration at 1 kHz. d) EO coefficient and e) impedance spectra of $Ba_{1-x}La_xTiO_3$ nanoparticle films as a function of modulation frequency.

The optical transmission spectra indicate that La doping does not appreciably influence the transmittance of nanoparticle films (Figure S2a, Supporting Information). We then investigated the effect of La doping on the EO performance of $Ba_{1-x}La_xTiO_3$ nanoparticle films. We found that at 1 kHz, the EO coefficient increases with increasing La concentration, reaching a maximum value of 42 pm V^{-1} at $x = 0.08$ (Figure 2c), twice that of the undoped sample.

Unfortunately, we observed that the EO coefficient decreases rapidly with increasing modulation frequency, a decrease that is faster at higher La concentrations (Figure 2d).

Prior reports suggest that a lower EO signal at high frequency may originate from ion migration.[15] We measured the impedance of the La-doped and undoped $BaTiO_3$ nanoparticle films. The capacitance of undoped $BaTiO_3$ does not change appreciably as the frequency is swept from 100 Hz to 1 MHz, indicating there is no noticeable ion migration. We hypothesized that the modulation bandwidth of the undoped $BaTiO_3$ might be limited by its higher capacitance. To explore this, we reduced the device's active area to lower the capacitance, and we found that the decreasing trend of EO with frequency is slowed down with the reduction in capacitance (Figure S10, Supporting Information). We thus attribute the frequency-dependent EO response of undoped $BaTiO_3$ to capacitive effects. Future studies could seek to reduce the measurement wavelength and the device area to enable investigations of the EO response and its bandwidth.

In contrast, the capacitance of La-doped $BaTiO_3$ drops rapidly at high frequencies (Figure 2e), with a similar frequency-dependence to its EO-dependence, hinting that ion migration might underlie each observation.

We propose that La^{3+} substituted at Ba^{2+} site causes charge imbalance and migration of oxygen vacancies, thus preventing the EO performance at high frequencies.

Transition metal favors the Ti site as acceptors, which is expected to compensate for charge imbalance. Our calculation of the Berry phase polarization predicts that Mn-doped $BaTiO_3$ enables the highest polarization of 32.85 Debye among acceptor dopants (Fe, Mg, Zn, Mn, Figure S7b, Supporting Information).

This motivated us to explore simultaneous substitution of La^{3+} on Ba^{2+} sites and Mn^{2+} on Ti^{4+} sites: our hope was to compensate for charge imbalance and thus reduce ion migration.

We first evaluated the ion migration barrier of oxygen vacancies (V_O) in undoped, La-doped, and La–Mn co-doped $BaTiO_3$ structures using density functional theory (DFT) calculations (**Figure 3**). In the La-doped models, two migration paths are considered. One is that the V_O migrates far from the La_{Ba} point defects (P_2); in this case, the V_O migration barrier (P_2: 0.83 eV) is approximately that of the pristine structure (0.83 eV). The other is that the V_O migrates around La_{Ba} point defects, resulting in a more dominant path within a reduced barrier of (P_3: 0.46 eV), indicating severe ion migrations in the La-doped models.

For the La–Mn co-doped models, even if we assume Mn doping occurs as a separated point defect (Figure 3c), the V_O migration barriers (P_4: 1.00 eV/P_5: 0.42 eV) are slighter higher than the La-doped models. Furthermore, if the Mn atoms are doped to form La_{Ba}+Mn_{Ti} defect pairs (Figure 3d), the V_O migration barriers (P_6: 0.85 eV/P_7: 0.59 eV) are predicted to be higher still. Therefore, reduced ion migration can be expected with simultaneous substitution of La^{3+} on Ba^{2+} sites and Mn^{2+} on Ti^{4+} sites.

We then prepared La–Mn co-doped $BaTiO_3$ nanoparticle films to study the impact of donor–acceptor co-doping on the EO properties. In this study, the content of La is fixed at $x = 0.08$ to maintain the high EO coefficient, and the Mn is added at Mn/La ratios of 0.1, 0.2, 0.4, and 1. XRD patterns show that all the samples exhibit tetragonal structure at room temperature (Figure S8b, Supporting Information).

We next characterized the EO coefficient for various Mn/La ratios. We found that at 100 kHz, the absolute value of the EO coefficient peaks at a Mn/La doping ratio of 0.1 (**Figure 4**a), with values of 20 to 21.1 pm V^{-1}, and then 29.3 pm V^{-1} for the undoped, La-doped, and La–Mn co-doped $BaTiO_3$ nanoparticle films, respectively (Figure 4b).

We found that the decrease of the EO response with frequency was suppressed even at a small Mn/La ratio of 0.1. With the further addition of Mn, the EO signal was essentially independent of the modulation frequency (up to ≈100 kHz) (Figure 4c and Figure S11a, Supporting Information). The impedance exhibits a similar trend as does the EO coefficient, whereas the co-doped material does not show a reduction in capacitance with frequency (Figure 4d and Figure S11b, Supporting Information). We suggest that the charge imbalance induced by the substitution of La^{3+} at the Ba^{2+} site is compensated by simultaneously substituting Mn^{2+} at the Ti^{4+} sites.

The Teng–Man reflection ellipsometry technique is used to characterize EO in thin-film samples. Prior studies have also used it to estimate the r_{33} tensor.[16] In actuality, the EO coefficient can be affected by transmission, multiple reflections, and the piezoelectric effect.[17] In this and prior works, the use of the same Teng–Man method to compare doped and undoped $BaTiO_3$ nanoparticle films provides insight into the impact of composite engineering of $BaTiO_3$ films on EO properties.

3. Conclusion

We report using different doping strategies to increase the EO coefficient and control modulation frequencies in $BaTiO_3$ nanoparticles. We explored a simple solution-processed approach to integrate the photonic structure of ABO_3 perovskite and achieved an EO coefficient of 42 pm V^{-1} in La-doped $BaTiO_3$ nanoparticle films. However, we find that the EO response falls off rapidly with frequency and demonstrated by impedance spectroscopy that this is associated with ion migration. DFT calculations suggest that further doping Mn^{2+} may increase the ion migration barrier, enabling us to prevent ion migration by introducing acceptor dopants to overcome the charge imbalance while maintaining a high EO coefficient. These findings show that compositional engineering in $BaTiO_3$ nanocrystals allows for controlling their physical and optical responses and sheds light on their potential in EO applications.

4. Experimental Section

Materials: 200 nm $BaTiO_3$ nanoparticles, 20 wt% dispersed in ethanol were purchased from US Research Nanomaterials, Inc. Lanthanum (III)

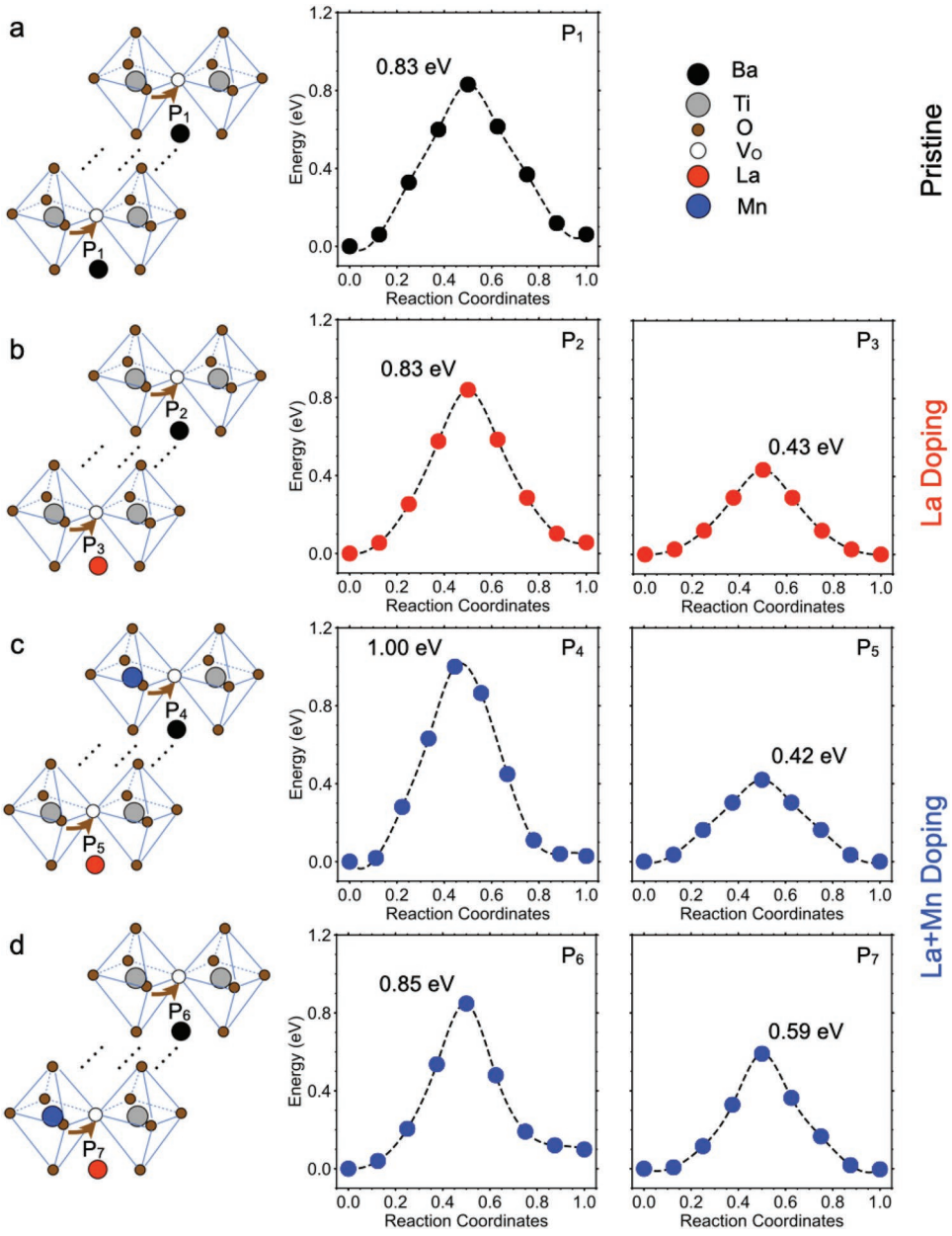

Figure 3. a–d) DFT calculated energy profiles of V_O migration in pristine $BaTiO_3$ (a), La-doped $BaTiO_3$ (b), and La–Mn co-doped $BaTiO_3$ (c,d). In (c), we consider La–Mn co-doping induces two separated point defects, while in (d) it exists in the form of near-neighbor defect pairs. The schematic plots of different migration paths are also shown.

chloride heptahydrate, manganese (II) acetate tetrahydrate were purchased from Sigma-Aldrich. All the chemicals were used directly as received.

Nanoparticle Film Preparation of Pristine $BaTiO_3$: The 20 wt% ethanol dispersion was first ultrasonicated for 60 min, and then diluted with ethanol in a 1:1 volume ratio. The uniform precursor was spin-coated onto the substrate with a speed of 2000 rpm for 30 s, and the resulted nanoparticle films were annealed at 250 °C for 30 min.

Nanoparticle Film Preparation of La-Doped and La–Mn Co-Doped $BaTiO_3$: The precursor solutions were prepared by dissolving stoichiometric lanthanum (III) chloride heptahydrate or manganese (II) acetate tetrahydrate in ethanol under continuous stirring. The resulting clear solutions were mixed with ultrasonicated 20 wt% ethanol dispersion in a 1:1 volume ratio. The mixture solution was then ultrasonic for 60 min to disperse evenly, and then spin-coated using the method mentioned above.

EO Device Fabrication: For the EO measurement, the ITO-coated glass substrate served as the anode, which was purchased commercially without further modification. The thickness of the coating was 145 ± 10 nm with high transmission of 85% at 1.55 µm, and the n and k values of the ITO electrodes at 1550 nm were $n = 0.976$ and $k = 0.792$ (Figure S3b, Supporting Information). The ITO electrodes were washed with deionized (DI)-H_2O, acetone, and isopropanol by ultrasonication for 30 min, followed by UV/ozone cleaning for 15 min. To prevent the current flow, a 30 nm Al_2O_3 insulating layer was deposited onto the ITO surface. Then, the doped and undoped $BaTiO_3$ nanoparticles were spin-coated onto the Al_2O_3 layer, respectively, using the abovementioned method. Finally, 140 nm-thick Ag was thermally evaporated on top of the $BaTiO_3$ films as the cathode.

Characterization: Thin films for XRD, transmission, and SHG measurements were prepared directly on glass substrates. XRD

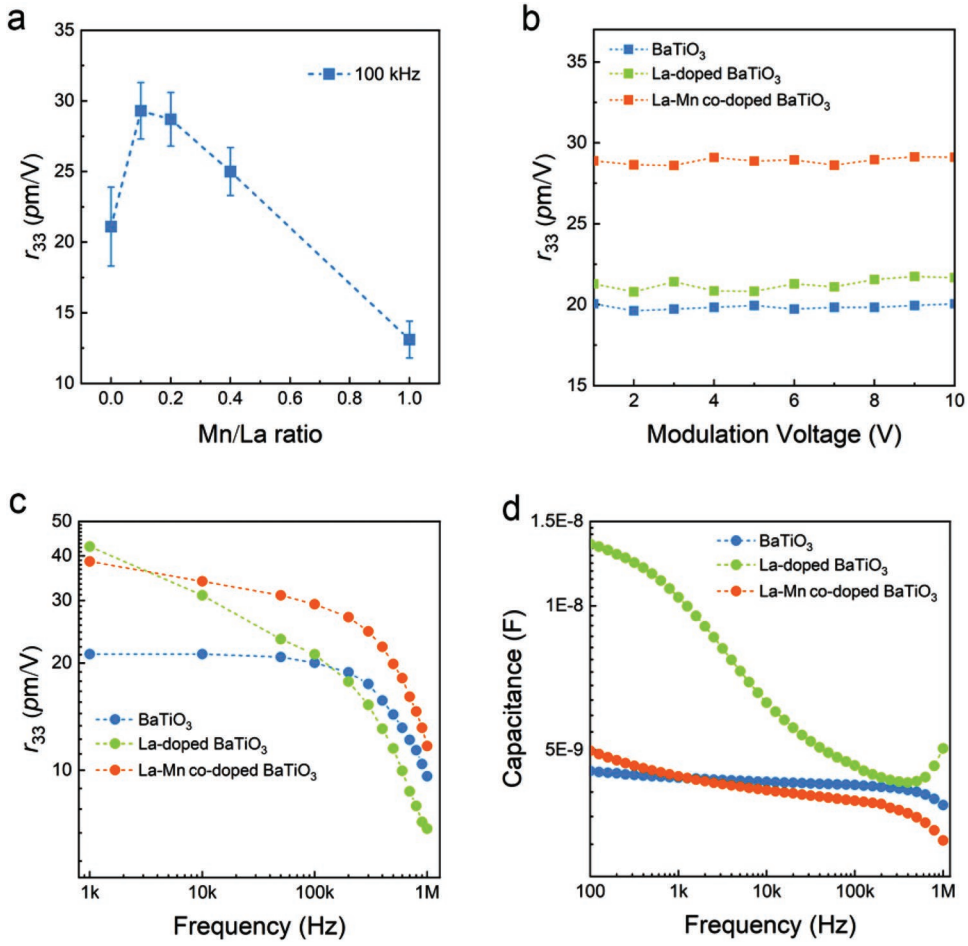

Figure 4. a) EO coefficient as a function of Mn/La ratio at 100 kHz. b) Comparison of the EO coefficient of the undoped, La-doped, and La–Mn co-doped $BaTiO_3$ nanoparticle films at 100 kHz. c) EO coefficient and d) impedance spectra as a function of the modulation frequency of the undoped, La-doped, and La–Mn co-doped $BaTiO_3$ nanoparticle films.

measurements were conducted using a Rigaku MiniFlex 600 diffractometer (Bragg–Brentano geometry) equipped with a monochromatized Cu Kα radiation source (λ = 1.5406 Å, 40 kV, and 15 mA). The transmission spectra were measured by a Lambada 950 UV–vis–NIR spectrometer. For SHG measurements, a 1030 nm fundamental (5 kHz) was produced by an ytterbium-doped potassium gadolinium tungstate regenerative amplifier. The beam was then sent through an optical parametric amplifier (Orpheus, Light Conversion) to generate the wavelengths 1510, 1530, and 1550 nm. Scattered light from the thin films was then collected through two lenses into a 400 µm multimode fiber (Thorlabs), which was sent to a USB2000+ spectrometer (Ocean Optics). Surface morphology was characterized by AFM (Agilent) and the TEM images were achieved on a Novel Functions of HF-3300. Films for XPS measurements were prepared directly on ITO-coated glass substrates. For XPS measurement, a Thermo Scientific K-Alpha system with Al Kα source was used for XPS analysis of Ba 3d, Ti 2p, O 1s, and La 3d chemical states. The impedance spectra of the thin films were measured using a potentiated electrochemical workstation (AUT50690, PGSTAT204, The Netherlands) with the frequency ranging from 1 MHz to 100 Hz. Ellipsometry measurements were performed on a Horiba Jobin Yvon UVISEL Ellipsometer in reflection mode with an incident spectrometer angle of 70°. The intensity functions were collected at energy increments of 0.1 eV across the spectral range of 0.6 to 4.5 eV.

Density Functional Theories: Unless otherwise noted, all the calculations were performed using the FHI-aims all-electron code.[18] The default numerical settings, referred to as "tight" in FHI-aims were used. Local minimum-energy geometries of the Born–Oppenheimer surface were obtained with residual total energy gradients below 1×10^{-2} eV Å^{-1} for atomic positions by Perdew–Burke–Ernzerhof (PBE)-generalized gradient approximations functional[19] within the vdW correction following the Tkatcheko–Scheffler method[20] (PBE+TS). For the simulation of ion migration, the $3 \times 3 \times 3$ supercells with $2 \times 2 \times 2$ k-mesh grid were employed. The initial and final structures were first relaxed by PBE+TS for the atomic positions and then fixed during migration. The growing string method was used to obtain the energy profile of migration images.[21] The convergence force was set to 0.2 eV Å^{-1} during minimum energy pathway optimization, within a tighter convergence force (0.05 eV Å^{-1}) for the climbing images to find the correct energy barriers. For the berry phase polarization calculations, all the doped structures were first relaxed by PBE+TS for the atomic positions by FHI-aims. Then the cp2k code[22] was used to calculate the berry phase polarization based on these relaxed structures within PBE functional. Goedecker–Teter–Hutter (GTH) pseudopotentials[23] and the corresponding TZVP-GTH basis sets were employed. The kinetic energy cutoff for the planewave expansions was set to 900 Ry.

Supporting Information

Supporting Information is available from the Wiley Online Library or from the author.

Acknowledgements

S.S.W. and T.Z. contributed equally to this work. This work was financially supported by Huawei Technologies Canada Co., Ltd. and the Natural Sciences and Engineering Research Council (NSERC). Computations were performed on the Niagara supercomputer at the SciNet HPC Consortium. SciNet was funded by the Canada Foundation for Innovation; the Government of Ontario; Ontario Research Fund – Research Excellence; and the University of Toronto.

Conflict of Interest

The authors declare no conflict of interest.

Data Availability Statement

The data that support the findings of this study are available from the corresponding author upon reasonable request.

Keywords

barium titanate, doping, electro-optic modulators, ion migration, nanoparticles

Received: August 9, 2022
Revised: September 7, 2022
Published online:

[1] C. Wang, M. Zhang, X. Chen, M. Bertrand, A. Shams-Ansari, S. Chandrasekhar, P. Winzer, M. Lončar, *Nature* **2018**, *562*, 101.

[2] a) A. D. Dupuy, Y. Kodera, J. E. Garay, *Adv. Mater.* **2016**, *28*, 7970; b) M.-J. Sun, C. Zheng, Y. Gao, A. Johnston, A. M. Najarian, P.-X. Wang, O. Voznyy, S. Hoogland, E. H. Sargent, *Adv. Mater.* **2020**, *33*, 2006368.

[3] a) S. Abel, F. Eltes, J. E. Ortmann, A. Messner, P. Castera, T. Wagner, D. Urbonas, A. Rosa, A. M. Gutierrez, D. Tulli, P. Ma, B. Baeuerle, A. Josten, W. Heni, D. Caimi, L. Czornomaz, A. A. Demkov, J. Leuthold, P. Sanchis, E. Fompeyrine, *Nat. Mater.* **2019**, *18*, 42; b) F. Eltes, C. Mai, D. Caimi, M. Kroh, Y. Popoff, G. Winzer, D. Petousi, S. Lischke, J. E. Ortmann, L. Czornomaz, L. Zimmermann, J. Fompeyrine, S. Abel, *J. Lightwave Technol.* **2019**, *37*, 1456; c) M. Cardona, *Phys. Rev.* **1965**, *140*, A651.

[4] a) M. A. Gomes, Á. S. Lima, K. I. B. Eguiluz, G. R. Salazar-Banda, *J. Mater. Sci.* **2016**, *51*, 4709; b) A. Karvounis, V. V. Vogler-Neuling, F. U. Richter, E. Dénervaud, M. Timofeeva, R. Grange, *Adv. Opt. Mater.* **2020**, *8*, 2000623.

[5] K. Uchino, E. Sadanaga, T. Hirose, *J. Am. Ceram. Soc.* **1989**, *728*, 1555.

[6] M. Mostafa, M. J. Rahman, S. Choudhury, *Sci. Eng. Compos. Mater.* **2019**, *26*, 62.

[7] W. F. Zhang, Y. B. Huang, M. S. Zhang, Z. G. Liu, *Appl. Phys. Lett.* **2000**, *76*, 1003.

[8] S. H. Wemple, M. DiDomenico, *J. Appl. Phys.* **1969**, *40*, 735.

[9] E. Kim, A. Steinbrück, M. T. Buscaglia, V. Buscaglia, T. Pertsch, R. Grange, *ACS Nano* **2013**, *7*, 5343.

[10] a) C. Kuper, K. Buse, U. Van Stevendaal, M. Weber, T. Leidlo, H. Hesse, E. Krätzig, *Ferroelectrics* **1998**, *208*, 213; b) Y. Y. Tang, P. F. Li, W. Y. Zhang, H. Y. Ye, Y. M. You, R. G. Xiong, *J. Am. Chem. Soc.* **2017**, *139*, 13903.

[11] C. C. Teng, H. T. Man, *Appl. Phys. Lett.* **1990**, *56*, 1734.

[12] F. Wang, E. Furman, G. H. Haertling, *J. Appl. Phys.* **1995**, *78*, 9.

[13] A. Zhang, Q. Li, D. Gao, M. Guo, J. Feng, Z. Fan, D. Chen, M. Zeng, X. Gao, G. Zhou, X. Lu, J. M. Liu, *J. Phys. D: Appl. Phys.* **2020**, *53*, 025301.

[14] K. K. Rahangdale, S. Ganguly, *Phys. B* **2022**, *626*, 413570.

[15] M. J. Sun, R. Sabatini, P. X. Wang, A. M. Najarian, K. Bertens, A. Johnston, S. Hoogland, E. H. Sargent, *Adv. Funct. Mater.* **2021**,*32*, 2107939.

[16] a) H. Xu, D. L. Elder, L. E. Johnson, Y. de Coene, S. R. Hammond, W. Vander Ghinst, K. Clays, L. R. Dalton, B. H. Robinson, *Adv. Mater.* **2021**, *33*, 2104174; b) M. B. M. Ahiheim, P. V. Bedworth, M. Blanchard-Desce, A. Fort, Z.-Y. Hu, S. R. Marder, J. W. Perry, C. Runser, M. Staehelin, B. Zysset, *Science* **1996**, *271*, 335.

[17] a) D. H. Park, C. H. Lee, W. N. Herman, *Opt. Express* **2006**, *14*, 8866; b) F. Michelotti, A. Belardini, M. C. Larciprete, M. Bertolotti, A. Rousseau, A. Ratsimihety, G. Schoer, J. Mueller, *Appl. Phys. Lett.* **2003**, *83*, 4477.

[18] a) V. Blum, R. Gehrke, F. Hanke, P. Havu, V. Havu, X. Ren, K. Reuter, M. Scheffler, *Comput. Phys. Commun.* **2009**, *180*, 2175; b) V. Havu, V. Blum, P. Havu, M. Scheffler, *J. Comput. Phys.* **2009**, *228*, 8367; c) X. Ren, P. Rinke, V. Blum, J. Wieferink, A. Tkatchenko, A. Sanfilippo, K. Reuter, M. Scheffler, *New J. Phys.* **2012**, *14*, 053020.

[19] a) J. P. Perdew, K. Burke, M. Ernzerhof, *Phys. Rev. Lett.* **1996**, *77*, 3865; b) J. P. Perdew, K. Burke, M. Ernzerhof, *Phys. Rev. Lett.* **1997**, *78*, 1396.

[20] A. Tkatchenko, M. Scheffler, *Phys. Rev. Lett.* **2009**, *102*, 073005.

[21] B. Peters, A. Heyden, A. T. Bell, A. Chakraborty, *J. Chem. Phys.* **2004**, *120*, 7877.

[22] The CP2K developers group, http://www.cp2k.org (accessed: September 2022).

[23] a) S. Goedecker, *Phys. Rev. B* **1996**, *54*, 1703; b) C. Hartwigsen, S. Goedecker, J. Hutter, *Phys. Rev. B* **1998**, *58*, 3641; c) M. Krack, *Theor. Chem. Acc.* **2005**, *114*, 145.